

Airborne measurements of CO₂ column absorption and range using a pulsed direct-detection integrated path differential absorption lidar

James B. Abshire,^{1,*} Haris Riris,¹ Clark J. Weaver,² Jianping Mao,² Graham R. Allan,³ William E. Hasselbrack,³ and Edward V. Browell⁴

¹NASA Goddard Space Flight Center, Greenbelt, Maryland 20771, USA

²Earth System Science Interdisciplinary Center, University of Maryland, College Park, Maryland 20740, USA

³Sigma Space Corporation, Lanham, Maryland 20706, USA

⁴STARSS-II Affiliate, NASA Langley Research Center, Hampton, Virginia 23681, USA

*Corresponding author: James.B.Abshire@nasa.gov

Received 31 January 2013; revised 25 March 2013; accepted 11 April 2013;
posted 6 May 2013 (Doc. ID 184647); published 21 June 2013

We report on airborne CO₂ column absorption measurements made in 2009 with a pulsed direct-detection lidar operating at 1572.33 nm and utilizing the integrated path differential absorption technique. We demonstrated these at different altitudes from an aircraft in July and August in flights over four locations in the central and eastern United States. The results show clear CO₂ line shape and absorption signals, which follow the expected changes with aircraft altitude from 3 to 13 km. The lidar measurement statistics were also calculated for each flight as a function of altitude. The optical depth varied nearly linearly with altitude, consistent with calculations based on atmospheric models. The scatter in the optical depth measurements varied with aircraft altitude as expected, and the median measurement precisions for the column varied from 0.9 to 1.2 ppm. The altitude range with the lowest scatter was 8–10 km, and the majority of measurements for the column within it had precisions between 0.2 and 0.9 ppm.

OCIS codes: (280.3640) Lidar; (300.6360) Spectroscopy, laser; (010.3640) Lidar; (140.3510) Lasers, fiber.

<http://dx.doi.org/10.1364/AO.52.004446>

1. Introduction

Although increasing atmospheric CO₂ is widely accepted as the largest anthropogenic factor causing climate change, there is considerable uncertainty about its global budget. To be useful in reducing uncertainties about carbon sources and sinks, space-based atmospheric CO₂ measurements need ~0.3% precision on spatial scales of $\leq 10 \times 10$ deg [1–3]. Several groups have analyzed space missions using passive spectrometers [4–6], and the GOSAT mission [7] is now making global CO₂ measurements from space using a Fourier-transform infrared spectrometer and reflected sunlight. However, sun angles restrict its measurements to the daytime and

midlatitudes. An inherent error source with space-based passive spectrometers is variability in path length caused by changes in surface elevation and by optical scattering from aerosols and thin clouds in the illumination or observation paths [8,9]. Scattering in either of these paths modifies the optical path length and thus the total CO₂ absorption viewed by these spectrometers, and so it can cause large retrieval errors even for thin cirrus clouds [10].

To overcome these limitations, the US National Research Council's 2007 Decadal Survey recommended a new space-based CO₂ measuring mission called ASCENDS [11]. Its goals are to produce global atmospheric CO₂ measurements using the laser absorption spectroscopy approach. The mission's goals

are to quantify the global spatial distribution of atmospheric CO₂ with 1–2 ppm accuracy, and to quantify the global spatial distribution of terrestrial and oceanic sources and sinks of CO₂ with approximately monthly time resolution. The ASCENDS approach offers continuous measurements over the cloud-free oceans, at low sun angles and in darkness, which are major advantages over passive sensors. The ASCENDS mission organizers held a workshop in 2008 to better define the science and measurement needs and plans for future work [12]. The European Space Agency (ESA) has also conducted mission definition studies for a similar space mission called A-SCOPE [3,13], and their lidar sensitivity and spectroscopic analyses have recently been published [14,15].

2. CO₂ Line Choice and Lidar Approach

The integrated path differential absorption (IPDA) lidar technique is widely used for open-path laser absorption spectroscopy measurements [16,17]. Typically two laser wavelengths are used, and the target is illuminated with the laser alternatively tuned onto and off the gas absorption line. The path-integrated gas absorption attenuates the on-line laser energy relative to the off-line wavelength. By measuring the optical depth of the gas absorption line, along with path length, and by knowing the difference in gas absorption cross sections, one can solve for the path-integrated gas number density. Several groups have measured atmospheric CO₂ using IPDA lidar, and summaries of prior work have recently been published [18,19].

The motivation for developing our airborne lidar [18,20–23] is to demonstrate a dual-wavelength pulsed IPDA approach as a candidate for the ASCENDS mission. The approach uses two tunable pulsed laser transmitters allowing simultaneous measurement of the absorption from a CO₂ absorption line in the 1570 nm band, O₂ extinction in the oxygen A-band, and surface height and atmospheric backscatter in the same path. A tunable laser is stepped in wavelength across a single CO₂ line for the CO₂ column measurement, while simultaneously a laser is stepped across a line doublet near 765 nm in the oxygen A-band for an atmospheric pressure measurement [24,25]. Both lasers are pulsed at a ~8 kHz rate, and the two absorption line regions are sampled in wavelength steps at typically ~1 kHz rate. The laser transmitters utilize tunable diode lasers followed by laser amplifiers. The direct-detection receiver measures the time-resolved laser backscatter from the atmosphere along with the energies of the laser echoes from the surface. After suitable averaging, the gas extinction and column densities for the CO₂ and O₂ gases are estimated from the sampled wavelengths of the surface-reflected line shapes.

We use a single line in the 1570 nm band for the CO₂ measurement [9]. This vibration-rotation band of CO₂ has an appropriate range of absorption that provides good sensitivity to the surface echo signal

and to variation in CO₂ in the lower troposphere. It also has minimal interference from other atmospheric species such as H₂O, and has several temperature-insensitive lines. The shorter wavelength lines in the *R* branch are a better match to available laser and detector technologies. The centermost line of the *R* branch at 1572.335 nm has been analyzed and is attractive for CO₂ measurements [26]. It has a low temperature sensitivity, particularly to temperature changes in the lower atmosphere.

Our approach samples the CO₂ line shape at multiple wavelengths. Nominally, eight are planned for space, while we have used both 20 and 30 for airborne measurements. Sampling at multiple wavelengths across the absorption line provides several capabilities and supports analysis using at least two vertical atmospheric weighting functions, which peak separately at lower and upper altitudes [26]. This approach also provides significant additional information that allows for solving for instrument parameters, such as baseline tilts, wavelength offsets, and wavelength-dependent lidar transmissions, which allows optimization of the measurements in subsequent analysis. To date we have used this for solving for wavelength offsets via a line-fitting process. We have also used it to characterize the lidar's response as a function of wavelength, which allows solving for and reducing the impacts of any residual wavelength variability. Oversampling the line in airborne lidar compared to space also allows postmeasurement analysis to vary the number of samples used and to help determine the optimum number.

Using pulsed lasers and receiver processing to time (and range) resolve the laser backscatter profiles allows postdetection signal processing to isolate the laser echo signals from the surface, and to reject backscatter from the atmosphere that arrives earlier. Hence it allows isolating the full column measurement from bias errors caused by atmospheric scattering [8,9]. Isolating the surface echo with a time gate in receiver processing also substantially improves the receiver's signal-to-noise ratio (SNR) by reducing the amount of noise from the detector and the solar background. For space missions, the photon efficiency of the lidar measurement technique is quite important. The photon efficiencies for three IPDA lidar approaches have recently been analyzed and compared [27] and the results showed that the pulse technique was quite efficient.

3. Airborne Lidar Description

In 2008 we adapted our ground-based lidar [20] for airborne use on the NASA Glenn Lear-25 aircraft, [28] shown in Fig. 1. The sensor head was mounted above the aircraft's nadir window. In initial flights [18], the etalon fringes from the aircraft's nadir camera window significantly limited the measurement precision. For the 2009 flights a custom pair of wedged and antireflection coated optical windows were used as a replacement, and they eliminated this issue.



Fig. 1. (Left) NASA Glenn Lear-25 aircraft. The nadir window assembly is just below the NASA logo. Photographs of the lidar installed on the aircraft showing the sensor head assembly (middle) and the dual aircraft racks (right).

The airborne lidar transmitter operates in pulsed mode by using an acousto-optic modulator (AOM) between the diode laser and the fiber amplifier. The receiver measures the time-resolved sum of 450 photon-counting lidar backscatter profiles each second, for each of the 20 laser wavelengths, with sufficient recording duration to include the surface echo signal. The airborne lidar specifications are listed in Table 1.

The approach for sampling the CO₂ line and lidar block diagram is shown in Fig. 2. The lidar signal source is a distributed feedback (DFB) laser diode, which is operated near 1572.33 nm by controlling its temperature and current. A ramp from a signal generator was used to sweep the current to the diode laser, and hence its output wavelength. The diode's CW output is then gated into pulses by an AOM to an erbium-doped fiber amplifier (EDFA). For these measurements, 20 wavelength samples are used

across the CO₂ line. A small percentage of the CW seed laser output is split off and directed through a fiber-coupled CO₂ absorption cell and to a detector. The CO₂ cell serves as a monitor for the center wavelength of the sweep. The nominal static transmitted laser pulse wavelengths are measured in a calibration procedure using a commercial wavemeter. Subsequent testing showed some curvature in the scanning dynamic ramp signal, so we used a more accurate quadratic functional model for the laser wavelength versus pulse sequence number in the data analysis.

The laser output is a sequence of 1 μ s wide laser pulses that occur at a 10 kHz rate. The collimated transmitted laser signal exits toward nadir through the window. The laser backscatter is collected by the receiver's 20 cm diameter Cassegrain telescope, which views nadir through another window in a bi-static configuration. A multimode fiber is used to couple the optical signal from the telescope focal plane to the receiver optics. After passing through an optical bandpass filter, the signal is focused onto a photomultiplier tube (PMT) detector. The PMT used in the 2009 flights had a single photon-counting efficiency of ~2% near 1570 nm. The electrical pulse output from the PMT was amplified and passed through a threshold detector.

The pulses from the receiver's PMT detector and discriminator are binned and accumulated by the multichannel scalar (MCS). The start time of the MCS sweep is synchronized with the trigger for the first laser pulse of the 20 and hence the start of the pulsed wavelength sweep. Each MCS sweep contains a time-resolved histogram of PMT pulse counts versus time (i.e., the laser backscatter profiles) for all 20 pulses. At the end of 0.9 s, each MCS bin contains the total receiver counts for the 450 laser sweeps. The receiver histogram record is then read and stored. The laser trigger and data acquisition are synchronized to timing markers from the GPS receiver, and data was stored every other second. The computer also digitizes other signals, including those from thermocouples distributed across the sensor head and electronic rack, the inertial guidance system output from the aircraft, and the GPS position and time. A nadir viewing video camera also records the visible image through the nadir window.

Table 1. 2009 Pulsed Airborne CO₂ Lidar Parameters

CO ₂ line center wavelength	1572.33 nm (typically)
Laser min & max wavelengths	1572.29 nm, 1572.39 nm
Laser wavelength steps across line	20 (these flights)
Laser wavelength change/step	~5 pm
Laser peak power, pulse width, energy	25 W, 1 μ s, 25 μ J
Laser divergence angle	100 μ rad (these flights)
Seed laser diode type	DFB: Fitel FOL15DCWD
Laser pulse modulator (AOM)	NEOS Model: 26035-2-155
Fiber coupled CO ₂ cell	80 cm path, ~200 Torr pressure
Fiber laser amplifier (EDFA)	IPG EAR-10K-1571-LP-SF
Laser line scan rate	450 Hz
Laser linewidth per step	~15 MHz
Receiver telescope	Cassegrain, $f/10$ (Vixen)
Telescope diameter	20 cm
Receiver FOV diameter	200 μ rad
Receiver optical bandwidth	800 pm FWHM
Receiver optics transmission	0.64
Detector PMT type	Hamamatsu H10330A-75
Detector quantum efficiency	2% (this device)
Detector dark count rate	~500 kHz
Receiver signal processing	Photon counting/histogramming
Histogram time bin width	8 ns
Receiver integration time	0.9 s per readout
Recording duty cycle	45% (0.9 s every 2 s)

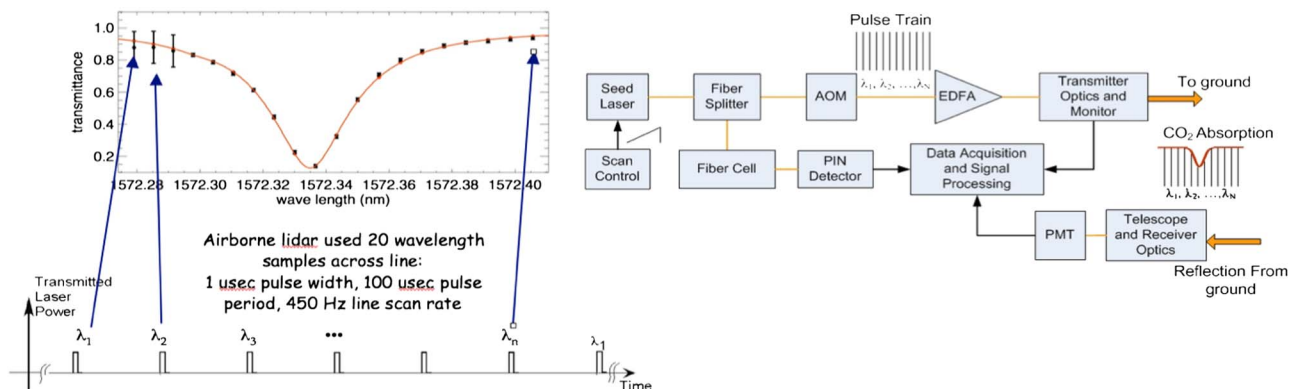


Fig. 2. (Left) CO₂ line sampling approach for airborne lidar. (Right) CO₂ lidar block diagram.

4. 2009 Airborne Campaigns

During mid-July through mid-August 2009, we flew an airborne campaign with a series of flights, each about 2.5 h long. We measured the shapes of the atmospheric CO₂ absorption line at stepped altitudes from 3 to 13 km over a variety of surfaces in Nebraska, the Department of Energy's ARM site in Lamont, Oklahoma, central Illinois, and near and over the Chesapeake Bay in North Carolina and Virginia's Eastern Shore Peninsula. These flights allowed testing and recording performance under different measurement conditions.

Strong laser signals and clear ground echo pulses and CO₂ line shapes were observed at all altitudes on most flights, and some measurements were made through thin and broken clouds. An example is shown in Fig. 3. It shows an echo pulse from the ground, whose sharp edges aid in range determination. It also shows time-resolved triple-echo pulses measured when viewing the ground over Ohio through two thin cloud layers. The first pulse in each triplet was the reflection from a cirrus cloud, while

the second was the reflection from a midaltitude cloud and the third was from the ground. The different amounts of CO₂ column absorption for different path lengths are evident. Without a range-resolved receiver, the echo pulse signals and measurements from the three different path lengths would be mixed. Using the pulsed measurement approach allows using range gating in the data processing to isolate the surface-reflected signals from the preceding atmospheric backscatter, and hence eliminates path-length errors from scattering.

After a series of test and checkout flights, four science flights were made in August. Diagrams of the flight's ground-track patterns are shown in Fig. 4, and the flight locations, flight patterns, and altitude ranges are summarized in Table 2. Three of the four flights were coordinated with the NASA LaRC/ITT Acclaim CO₂ lidar team. They provide measurements from the AVOCET *in situ* sensor [29,30] and special radiosondes launched close to the time of the airborne CO₂ lidar overpasses. These flights permitted comparisons of measurements made at

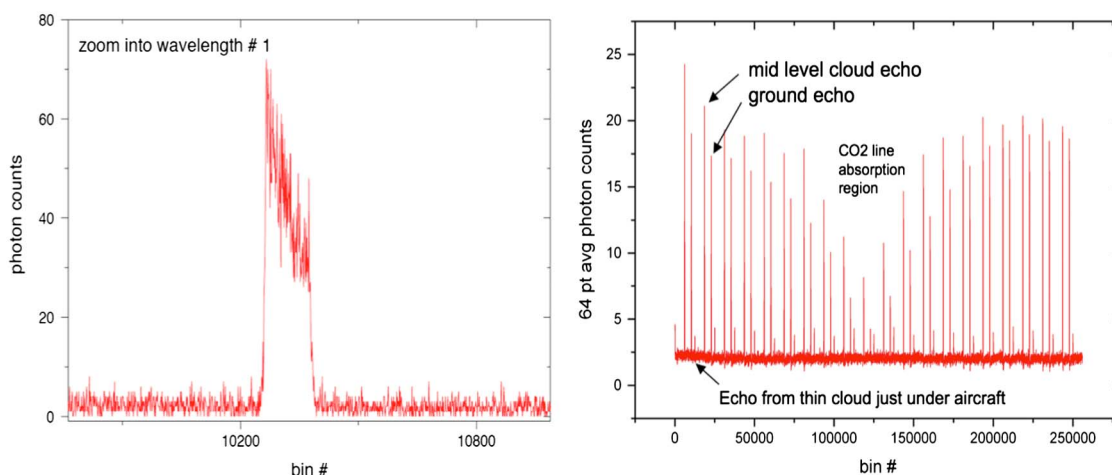


Fig. 3. (Left) Typical laser pulse shape reflected from the ground as recorded by the photon-counting receiver. This was from accumulating 450 individual ground echoes integrated (histogrammed) over 0.9 s. (Right) Example of a raw (uncorrected) recorded backscatter profile when measuring to the ground through two thin cloud layers. It shows three time-displaced echo pulses per transmitted pulse. The smallest initial echo pulses are from the cirrus clouds just under the aircraft. The figure also shows the two range-displaced CO₂ column absorptions that are evident in the echoes from the midlevel cloud layer and the deepest absorption in the longest path to the ground.

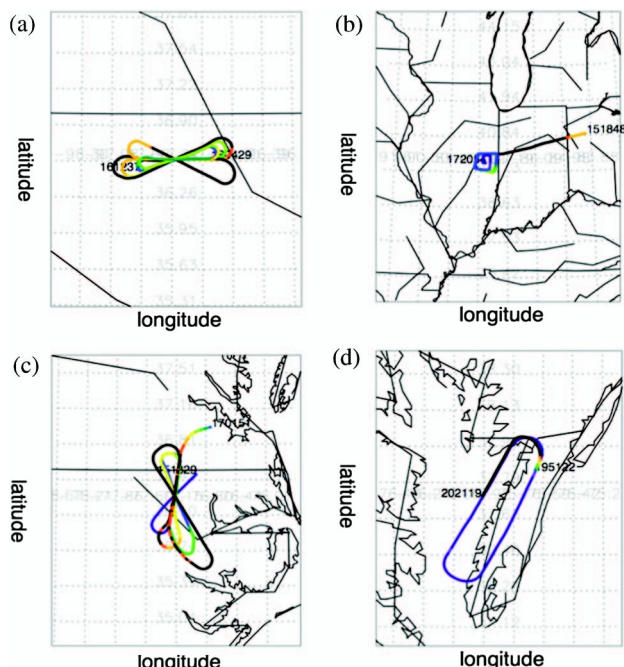


Fig. 4. Maps of the ground-track patterns for the flights analyzed: (a) ARM-4, (b) Illinois, (c) North Carolina, and (d) Virginia. The flight locations and other parameters are summarized in Table 2.

different altitudes and differential optical depths (DODs) to those calculated from *in situ* measurements and using the spectroscopic parameters for the CO₂ line from HITRAN 2008.

5. Airborne CO₂ Measurements and Calculations

In order to estimate the actual CO₂ column density during the flights, measurements of atmospheric temperature, moisture, and pressure vertical profiles were used from the radiosonde balloons, which were launched near the flight location. Their parameters were used in a 40-layer atmospheric model to compute dry air column density versus height to 13 km altitude. The airborne flights were also coordinated with LaRC investigators, and the flights over the ARM site, North Carolina, and Virginia were underflown with *in situ* gas measurements made from the NASA LaRC UC-12 aircraft. This used the NASA LaRC atmospheric vertical observation of CO₂ in the Earth's troposphere (AVOCET) gas

analyzer to measure CO₂ concentrations. It sampled air and CO₂ concentrations every second from takeoff to 8 km, the UC-12's upper flight altitude, and back to the ground. When the spiral was performed over an airport, the *in situ* measurements were obtained down to the ground via a "touch and go" of the airport runway.

All AVOCET measurements were references to GPS latitude, longitude, and altitude measurements made on the UC-12. The spirals were timed to coincide with overflights of the GSFC CO₂ sounder. Vaisala RS-92 radiosondes were also launched during the Oklahoma, North Carolina, and Virginia flights to obtain the meteorological parameters needed for converting the CO₂ mixing ratios measured by AVOCET to the path-integrated CO₂ column density needed to compare with the lidar. The RS-92 radiosondes have pressure, temperature, and relative humidity absolute accuracies from 1080 to 1100 hPa of 1 hPa, 0.5°C, and 5%, respectively. These radiosondes were launched from the ground at the center of the UC-12 spiral location, and when possible, they were launched at the completion of the UC-12 spiral. The activities of the UC-12, Lear-25, and ground radiosonde personnel were coordinated to ensure the most coincident data acquisition for comparison of the *in situ* derived CO₂ data and the lidar measurements.

Based on these readings, the CO₂ line shapes, the CO₂ column number density, and the averaged two-way DOD for the 1572.335 nm line were computed versus flight altitude for each flight. These calculations provided a reference comparison for the airborne lidar measurements and showed how the CO₂ line shapes and depths should vary with flight altitude and range to the surface. A summary of the airborne concentration measurements, and the computed CO₂ column density, is plotted in Fig. 5. They show that the CO₂ mixing ratio was similar for three of the four flights.

Over Illinois the AVOCET reading was not available, so an analysis was used based on the nearest ground-based *in situ* sensor, which indicated a ~30 ppm CO₂ reduction near the surface due the growing surrounding crop land. Figure 5 also shows the CO₂ number density plotted versus altitude, as a difference from the US standard atmosphere with

Table 2. Summary of 2009 Science Flights

Notation	ARM-4	Illinois	North Carolina	Virginia
Location	Lamont, OK	Homer, IL	Ahoski, NC	Melfa, VA
Flight dates (all 2009)	August 4	August 13	August 17, am	August 17, pm
Flight pattern	Bowtie	Box	Bowtie	Racetrack
Surface elevation (m)	315	178	30	15
Surface pressure (mbar)	974	998	1021	1020
Altitude change in flight	Ascending	Descending	Ascending	Ascending
Primary altitude range (km)	3.0–12.6	12.6–5	4.9–11.5	4.9–11.5
Altitude step size (km)	1.5	2.5	1.5	1.5
Number of altitude steps	10 (3 repeated)	3	5	5
Time span of data record (s)	6300	3400	4500	6000

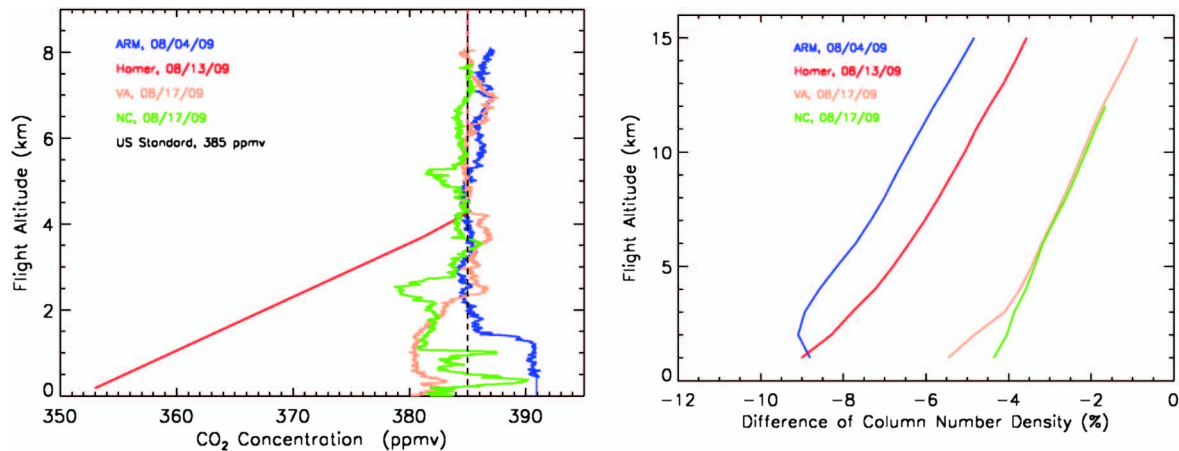


Fig. 5. (Left) *In situ* CO₂ measurements from Avocet for the four flights in August 2009: ARM-4, Illinois, North Carolina, and Virginia. (Right) Computed CO₂ column density versus altitude above the surface for the four flights, minus that of the US standard atmosphere with a 385 ppm mixing ratio. The primary differences in the plots are caused by the different average column air densities caused by the different surface elevations of the flight locations.

a constant 385 ppm mixing ratio. It clearly shows that the conditions of warmer dry air at lower pressure during the ARM and Illinois flights reduced their dry air density and hence their total column CO₂ compared to the later East Coast flights. The AVOCET instrument also sampled water vapor, and the column-integrated water vapor mixing ratio is plotted in Fig. 6 for all flights. In this plot the measurements for the Homer, Illinois flight were provided by a nearby radiosonde. The results show that in the air columns measured in the flights, the water vapor mixing ratios were similar and varied smoothly from ~2% near the surface to ~0.5% for columns with upper endpoints near 12 km.

For this analysis, we first performed a line fit, as described in the section below, based on all 20 measurement wavelengths. We then report the DOD on the fitted line where the on-line wavelength is set to the line peak, and the off-line wavelengths are

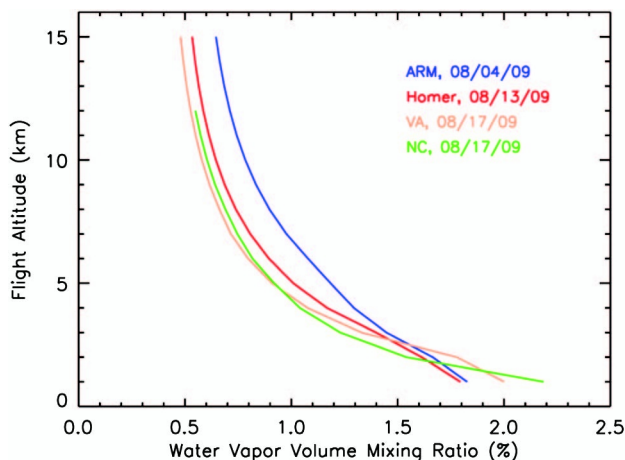


Fig. 6. Plot of the path-integrated water vapor in the CO₂ measurement column for the four flights as a percentage of the dry air column. The water vapor was measured by the aircraft *in situ* sensor in the spiral segments of their flights, except for Homer, Illinois, where it was measured by a nearby radiosonde.

in the wings. Specifically for these flights we computed and report

$$\text{DOD}(pk) = \text{OD}(\lambda_{pk}) - \{\text{OD}(\lambda_{pk} - \Delta\lambda) + \text{OD}(\lambda_{pk} + \Delta\lambda)\}/2, \quad (1)$$

where the OD values are measured on the fitted line shapes, and the off-line ODs are measured at offsets $\Delta\lambda = 100$ pm from the line peak, as shown in Fig. 7. For these choices of wavelengths, calculations from a layered atmospheric model shown in Fig. 8 show the DOD(pk) varies almost linearly with altitude.

6. CO₂ Measurement Processing

For the flights the lidar recorded the time- and wavelength-resolved laser backscatter with 0.9 s integration time. In subsequent analysis, the line shape measurements at each flight altitude step were averaged with 2–10 measurements/average. We used a CO₂ line retrieval approach, shown in Fig. 9, based on the Gauss–Newton method [31] to analyze each altitude averaged line shape. This approach has sufficient free parameters to model and correct for instrument effects, to fit the resulting CO₂ line shapes, and to estimate the corresponding CO₂ column densities and optical depth at each altitude. The CO₂ retrieval algorithm yields an estimate of the mean CO₂ column density over the laser path length based on line absorption strength taken from the HITRAN 2008 [32] database. The input observations were ratios of the photon counts in the surface echo signals at each wavelength after they were normalized by an estimate of transmitted pulse energy. The error covariance matrix for the observed signals was diagonal and equally weighted for all but the first three wavelengths. Examples of calculated and observed (retrieved) line shapes for flights over the ARM site and over North Carolina are shown in Fig. 7.

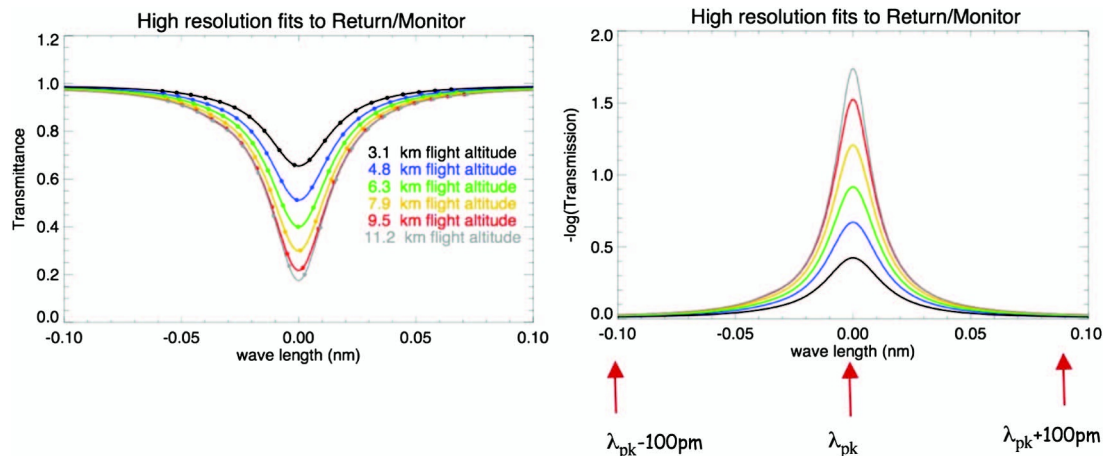


Fig. 7. Example plots from the line fitting and analysis approach. (Left) Examples of measured wavelength samples (dots) and fitted line shapes in transmission (solid curves) overlaid for averaged measurements above North Carolina from 3.1 to 11.2 km altitudes, which are color-coded. The wavelength axis is centered on the line peak. (Right) Computed line shapes in optical depth (OD) for the corresponding colors on left-hand plot. The three wavelength samples used for the 2009 flight analysis are indicated.

The algorithm requires several other inputs. First are estimates of the vertical profile of temperature, pressure, and water vapor versus altitude. These are used to calculate the approximate CO₂ line shape, and were estimated from gridded meteorological fields from the Goddard Modeling and Assimilation Office for the locations at the time of the flights. They are used to calculate the wavelength-resolved absorption spectra of atmospheric CO₂ based upon HITRAN 2008 for each 1 km altitude bin.

The range to the surface must be known to compute the volume density of atmospheric CO₂ from the measurement of DOD of the column. Our lidar processing does this by recording the trigger time of the laser pulse emissions and by computing an estimate of the reflectance time of the echo pulse. We use a cross-correlation algorithm to optimize the range determination. Recent analysis [23] has shown this usually produces estimates with uncertainties of a few meters over most surfaces.

The signal consisted of the detected photons in each pulse of the wavelength scan. The algorithm adjusted the computed column average CO₂ density (and mixing ratio) to minimize the error between the computed line shape and that sampled by the lidar. It does this also using an instrument model that allows degrees of freedom in several model variables. For these experiments, the lidar's wavelength (i.e., wavelength per laser pulse number) was modeled as a quadratic function, and the three wavelength coefficients were solved for, using the ground wavelength calibration as a prior constraint. The lidar's baseline response, or system transmission, was also allowed to vary with wavelength via a quadratic dependence with pulse number. This can change during flight due to the changing aircraft cabin temperature and pressure. Using this approach to simultaneously determine CO₂ density and instrument model parameters considerably improved the measurement accuracy by solving and correcting

for slowly varying instrument offsets and nonlinearities. The result was that the residual difference between the fitted CO₂ lines and lidar measurements on all flights was small, and the average rms difference per wavelength sample varied between 0.7% and 1.7%.

7. Expected Measurement Performance

The error of the lidar measurement of optical depth and path-integrated number density depends on its signal and noise characteristics and the magnitude of bias errors. A simplified treatment for this approach [18], for a uniform atmospheric path and target at a fixed range R , illustrates some important

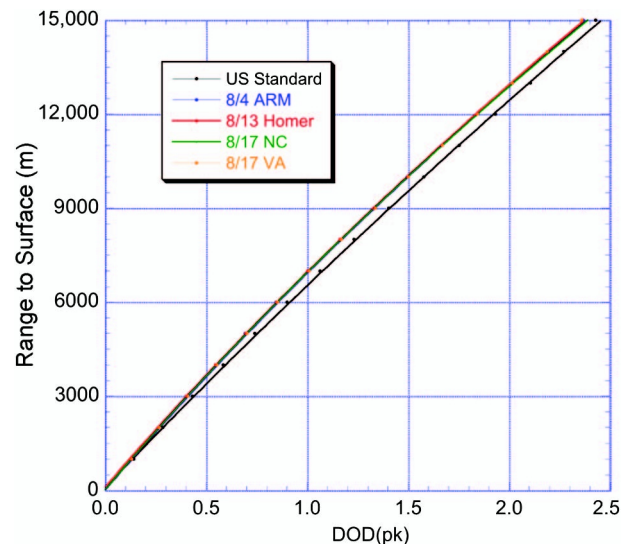


Fig. 8. Computed DOD(pk) versus altitude for the 2009 flights, based on *in situ* readings of dry air and CO₂ concentrations and using HITRAN 2008 spectroscopy. The shapes of the DOD(pk) for all the locations are quite similar, and vary quadratically (nearly linearly) with range. A computation based on the US standard atmosphere 385 ppm mixing ratio is also shown. Since it has a higher dry air density, it has a larger DOD at a given altitude.

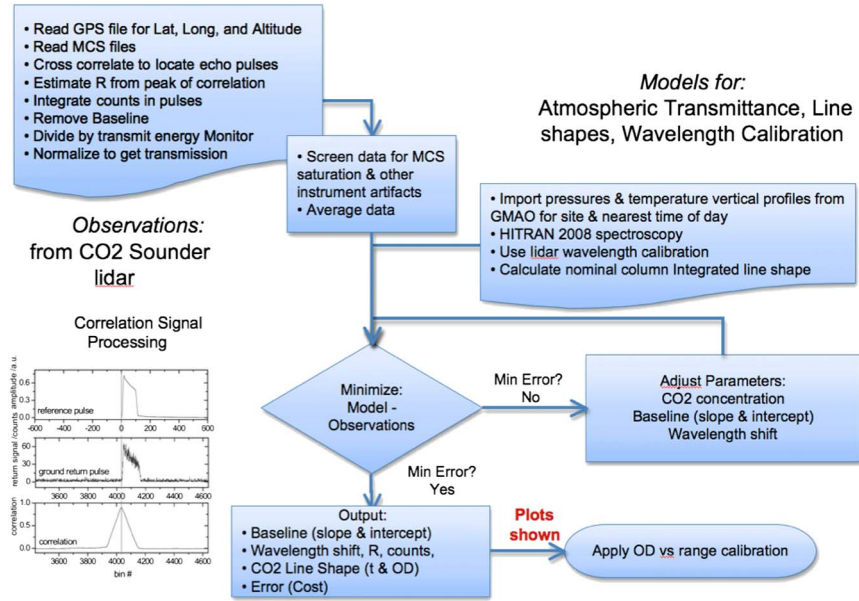


Fig. 9. Algorithm used to process the 2009 airborne lidar measurements.

dependencies. A complete analysis must account for many factors, including variability in the lidar parameters, atmospheric temperature and pressure, laser speckle, changing surface reflectivity and range, etc. [14,15].

This campaign was the first one in which this lidar was fully functional over the full range of measurement altitudes. During it, the lidar's operational modes were still being optimized, and so factors such as laser power, detector gain settings, and receiver discriminator settings were varied during the flights, and from flight to flight. These operational settings changed the instrument responses, and hence changed the measurement offsets (or biases) for the flights. Hence in this paper we focus on analyzing the random errors in the measurements.

For vertical measurements made with the on-line signal near the absorption peak, we can assess the primary impacts of random errors starting with the derivation given in Appendix A. The primary result is that the near surface number density and volume mixing ratio can be estimated from

$$n_1(0) = X_{\text{CO}_2} n_2(0) = \alpha_1 \frac{\text{DOD}_1(z_s, Z)}{R_1}, \quad (2)$$

where $\alpha_1 = 1/\{2[\bar{\sigma}_1(\lambda_{\text{on}}, 0) - \bar{\sigma}_1(\lambda_{\text{off}}, \overline{Z - z_s})]\}$, the range to the surface, $R_1 = Z - z_s$, and the other terms are defined in Appendix A. Equation (2) is consistent with the results from the absorption calculations shown in Fig. 8 that were based on a layered atmospheric model. They show for $\lambda_{\text{on}} = \lambda_{\text{pk}}$ and λ_{off} well off peak that the values of DOD(pk) varied almost linearly with range $R = Z - z_s$.

The impact of errors in the airborne lidar measurements can be determined from Eq. (2). If the individual measurement precisions of DOD and R are high, then the errors in the measurements, Δ , are small

relative to their mean values. For this case, one can write the individual measurements as additive deviations (errors) around their mean values, so that

$$\begin{aligned} n_i &\approx \bar{n}_i \left(1 + \frac{\Delta n_i}{\bar{n}_i} \right), \\ \text{DOD}_i &\approx \overline{\text{DOD}}_i \left(1 + \frac{\Delta \text{DOD}_i}{\overline{\text{DOD}}_i} \right), \quad \text{and} \\ R_i &\approx \bar{R}_i \left(1 + \frac{\Delta R_i}{\bar{R}_i} \right). \end{aligned} \quad (3)$$

Since the deviations are small and have mean values equal to 0, the mean value for the CO₂ density can be approximated as

$$\bar{n}_1 = \alpha_1 \frac{\overline{\text{DOD}}_1}{\bar{R}_1}. \quad (4)$$

For these experiments the errors in the dry air densities are assumed to be much smaller than for CO₂. Therefore relative error in the number density (2) is similarly

$$\left(\frac{\Delta n_1}{\bar{n}_1} \right) \approx \left(\frac{\Delta \text{DOD}_1}{\overline{\text{DOD}}_1} \right) - \left(\frac{\Delta R_1}{\bar{R}_1} \right), \quad (5)$$

and the corresponding relative statistical error is

$$\frac{\sigma(\Delta n_1)}{\bar{n}_1} = \sqrt{\frac{\sigma^2(\Delta \text{DOD}_1)}{(\overline{\text{DOD}}_1)^2} + \frac{\sigma^2(\Delta R_1)}{(\bar{R}_1)^2}}, \quad (6)$$

where $\sigma^2(x)$ is the variance of x and $\sigma(x)$ is its standard deviation.

With our airborne lidar, the random error in range was typically 2–5 m. The relative error in range varied from 0.1%, at 2 km altitude, to ~0.05% at 10 km. These relative errors are much smaller than those for DOD, so the measurement errors in DOD dominate. For this case, the fraction error of the total column CO₂ number density can be written as

$$\frac{\sigma(\Delta n_1)}{\bar{n}_1} = \frac{\sigma(\Delta \text{DOD})}{\overline{\text{DOD}}} = \frac{1}{\overline{\text{DOD}}} \cdot \left(\frac{1}{\overline{\text{SNR}}_{\text{off}}} + \frac{1}{\overline{\text{SNR}}_{\text{on}}} \right). \quad (7)$$

Since the airborne lidar scans the CO₂ line at a frequency f_{las} and averages for an integration time T_{int} , the total number of pulse measurements averaged is $M = f_{\text{las}} \cdot T_{\text{int}}$. The average SNRs for the off- and on-line wavelengths are

$$\overline{\text{SNR}}_{\text{off}} = \sqrt{M} \frac{N_s(\lambda_{\text{off}})}{\sqrt{N_s(\lambda_{\text{off}}) + 2N_n}} \quad (8)$$

and

$$\overline{\text{SNR}}_{\text{on}} = \sqrt{M} \frac{N_s(\lambda_{\text{on}})}{\sqrt{N_s(\lambda_{\text{on}}) + 2N_n}}, \quad (9)$$

where N_n represents the detected background and dark counts accumulated over the laser pulsewidth for each laser firing, and N_s represents the detected signal photons for that wavelength for each laser firing.

The relative error varies significantly with range. As for most IPDA lidar, the CO₂ absorption for measurements at λ_{on} reduces the detected signal compared to λ_{off} , so that SNR_{on} is usually the limiting error source. For this case Eq. (7) simplifies to

$$\frac{\sigma(\Delta \text{DOD})}{\overline{\text{DOD}}} = \frac{1}{\overline{\text{DOD}}} \cdot \left(\frac{\sqrt{N_s(\lambda_{\text{on}}) + 2N_n}}{\sqrt{MN_s(\lambda_{\text{on}})}} \right). \quad (10)$$

Since for the wavelengths chosen $\text{OD}_{\text{on}} \gg \text{OD}_{\text{off}}$,

$$\overline{\text{DOD}} \approx \text{OD}_{\text{on}} = \frac{\bar{n}_1(0) \cdot R}{\alpha_1}. \quad (11)$$

When the lidar measurement is also signal shot noise limited, Eq. (10) becomes

$$\frac{\sigma(\Delta \text{DOD})}{\overline{\text{DOD}}} = \frac{\exp(\bar{n}_1(0) \cdot R/2\alpha_1)}{\bar{n}_1(0) \cdot R/\alpha_1} \frac{1}{\sqrt{MN_s(\lambda_{\text{off}})}}. \quad (12)$$

Equation (12) summarizes the effect of varying range and off-line signal levels on the relative error. For these experiments, the maximum count rate of the photon-counting receiver was limited to prevent saturation. This limited the value of $N_s(\lambda_{\text{off}})$ in Eq. (12) at lower altitudes, where the optical depth of the absorption is also small. Hence for low altitudes the $1/R$ term in Eq. (12) magnifies the errors

from the finite SNR. At higher altitudes, the on-line signal varies as $\exp(-R)$, and so the relative error at high altitudes increases as $\exp(R/2)$. Since the relative error has limits that grow at both lower and upper altitudes, there is an altitude band with minimum errors, which for these experiments was 8–10 km.

8. Airborne Measurement Results and Discussion

After data processing, the airborne measurements per site were summarized in a common format for all four flights, and were plotted versus flight location. The DOD(pk) values determined from the 0.9 s integration time were plotted versus the time of flight, along with the range estimates (R) to the surface. The same DOD(pk) values are plotted versus R to assess the linearity and scatter of the measurements versus altitude. Other analysis of the 2009 flights showed that the average signal levels follow predicted values [33], and that the altimetry measurements over water had an uncertainty of <3 m [23].

The 0.9 s measurements of DOD and range are plotted versus elapsed time for each flight in Figs. 10(a), 12(a), 14(a), and 16(a). Generally they show the range measurements and DOD(pk) varied together as expected on all flights, with the DOD(pk) and range being stable in the straight segments and both increasing due to the longer slant path ranges during the aircraft turns. The DOD(pk) readings have more scatter for measurements above 9 km. The DOD is plotted versus slant range for each of the flights in Figs. 10(b), 12(b), 14(b), and 16(b). The plots show the DOD generally followed the range as predicted for all flights, and the DOD estimates have more scatter at ranges above 9 km. This is expected due to both the larger R^2 signal losses and the greater CO₂ on-line absorption for the longer columns.

To determine statistics, for each flight the measurements were then segmented into groups of 100 s time duration. For the recording period of 2 s, these groups could have at most 50 individual (0.9 s duration) measurements. Screening criteria were then applied based on pulse energy, range, DOD, and others to remove outliers. Limiting the maximum spread in range worked well to remove measurements made in aircraft turns. Typically 30–35 measurements survived screening in the groups.

From these the mean values, standard deviations and relative errors were computed and plotted versus altitude. To allow assessing the equivalent measurement precision in an equivalent mixing ratio, the relative errors in the DOD values in Eq. (12) were scaled to equivalent errors in X_{CO_2} by using

$$\sigma(\Delta X_{\text{CO}_2}) = \bar{X}_{\text{CO}_2} \cdot \frac{\sigma(\Delta n_1)}{\bar{n}_1} = \bar{X}_{\text{CO}_2} \cdot \frac{\sigma(\Delta \text{DOD})}{\overline{\text{DOD}}}. \quad (13)$$

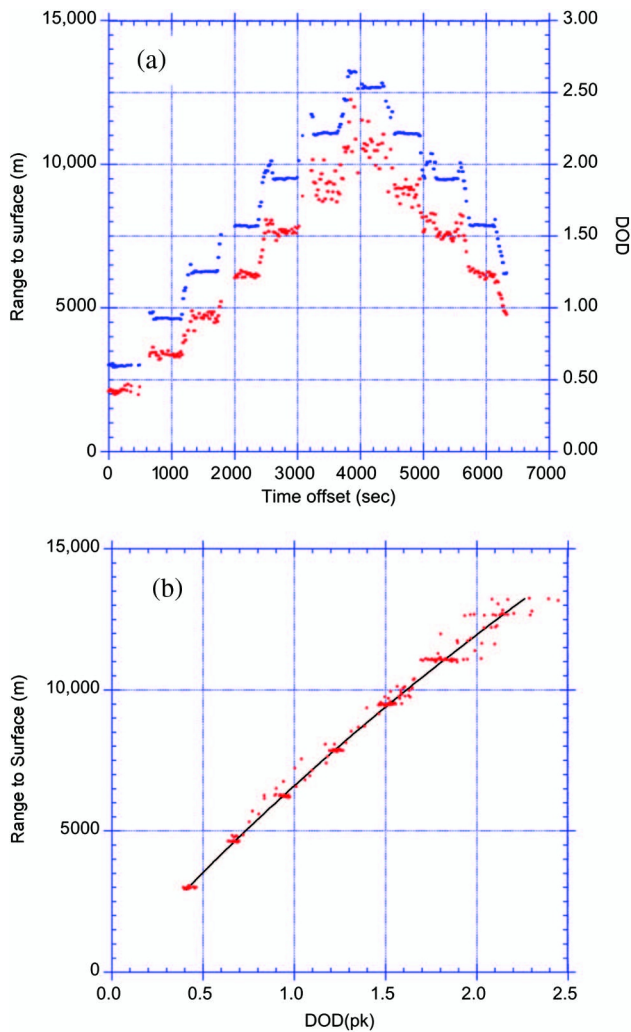


Fig. 10. Measurements from the flight above DOE ARM site. (a) Lidar measurements of range to surface (blue dots, left-hand axis) and DOD(pk) (red dots, right-hand axis) versus time for the same flight. The stair step changes in altitude are evident, and the DOD(pk) values follow the range until ~ 8 km, and then have more scatter above 8 km. A total of 1747 measurements (each 1 s) were made. (b) Same lidar measurements of DOD(pk) plotted versus measured range to the surface. The line shown is a best quadratic fit to the measurements. The measurements show a good fit to the line, with more scatter above 10 km.

This approach assumes the relative error in the measured CO_2 column absorption is much larger than that computed for the dry air column. Based on the airborne *in situ* measurements shown in Fig. 5, \bar{X}_{CO_2} was taken to be 385 ppm. These relative errors were plotted versus range in Figs. 11(a), 13(a), 15(a), and 17(a). These plots show a significant dependence on the column length, as is expected from Eqs. (12) and (13). For ranges < 8 km, the DOD is smaller and so the errors scale inversely with range. At ranges > 10 km, the lidar has a declining signal strength range, due to both the R^{-2} factor and on-line gas absorption, and so the random errors increase with altitude. As a consequence, in all flights the altitudes with minimum relative errors were 8–10 km.

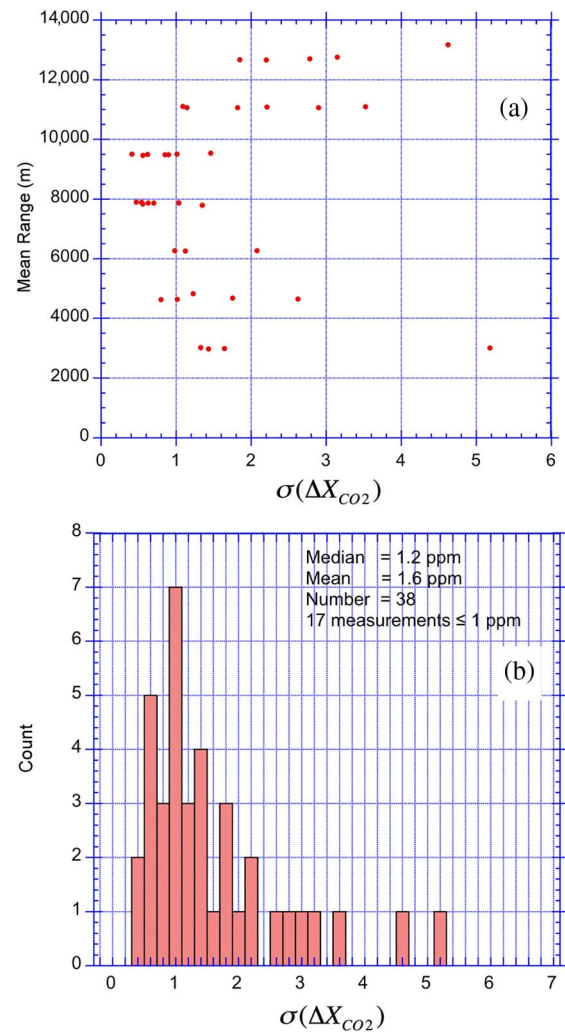


Fig. 11. Analysis of measurements from flight over ARM site. (a) Distribution of random errors calculated as $\sigma(X_{\text{CO}_2})$ versus altitude for measurements grouped every 100 s and for selected standard deviation (R) < 100 m. For low altitudes, the relative error increases because of a lower mean (DOD), while for upper altitudes the error increases due to declining received photons. The altitude with least scatter was 8–10 km, which had values of ~ 0.5 ppm. (b) Histogram of the same statistic for all altitudes. There were 38 groups, and the median error was 1.2 ppm.

For this optimum altitude band most errors were between 0.2 and 0.9 ppm. Histograms of relative errors for all ranges are plotted in Figs. 11(b), 13(b), 15(b), and 17(b). The lidar performance was similar on all flights, and some statistics from the analysis are summarized in Table 3.

An analysis of the range measurements is also summarized in Table 3. It summarizes the range variability within the groups. This was primarily determined by the variability of the surface topography in the ~ 14 to 18 km distances traversed by the aircraft during the data accumulation time of 100 s for the groups. At higher altitudes the aircraft speed was higher and so the distances were longer. The flights over Illinois and North Carolina were similar with median range standard deviations of 16.7–19 m.

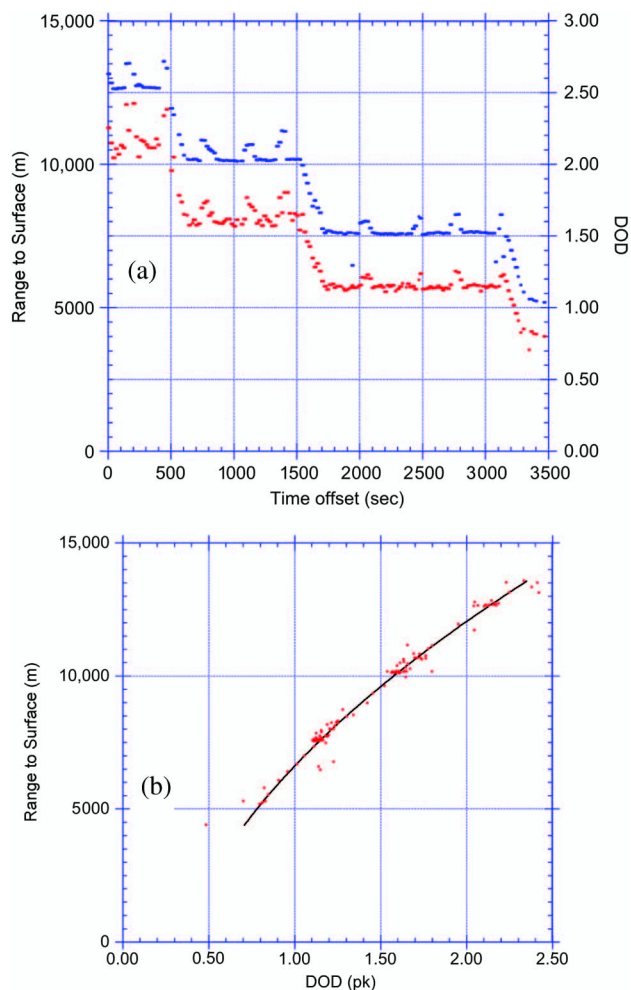


Fig. 12. Results from measurements from flight over Illinois. (a) Time history of lidar measurements of range to the surface (blue dots) and DOD(pk) (red dots). The increased range and increased DOD for the measurements during the turns (aircraft banks) at the corners of the box pattern are evident. (b) Plot of measured DOD(pk) versus measured range for the flight above Illinois. The line shown is a best quadratic fit to the measurements.

The ARM-4 flight and the Virginia flight were also similar with median values of ~ 10 m. The ARM site had a minimum range standard deviation of 3 m, while the Virginia flight, which was partially over the flat Chesapeake Bay water surface, had a minimum range standard deviation of 1 m. For the 8–10 km altitudes where performance was best, the relative range variability was small, and the dominant error was measuring DOD(pk).

9. Summary

During the summer of 2009 we demonstrated airborne lidar measurements of CO_2 absorption and column abundance using a pulsed direct-detection lidar based on the IPDA technique. Measurements were made at altitudes from 3 to 13 km over four locations and some through cirrus clouds. They showed clear absorption line shapes, which increased in optical depth with increasing aircraft altitude. The

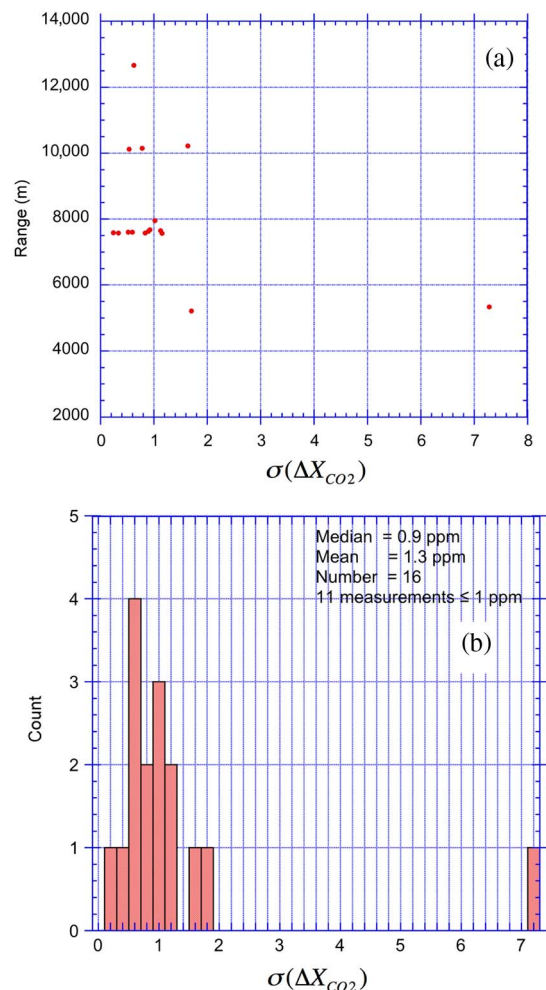


Fig. 13. Analysis of measurements from flight over Illinois. (a) Altitude dependence of $\sigma(X_{\text{CO}_2})$ calculated for measurements. Measurements were evaluated in groups of 100 s elapsed time and screened for only those groups whose standard deviation (range) is < 100 m. Typically each group has 32 measurements. (b) Histogram of the same statistic for all altitudes. There were 16 groups with a median error of 1.3 ppm and 11 groups with errors ≤ 1 ppm.

instrument's line shapes were estimated via a CO_2 line shape retrieval algorithm, which permitted solving and correcting for known instrument factors. The postprocessed line shapes agreed well with ones calculated from *in situ* measurements and radiosondes. The residual difference between the fitted CO_2 lines and lidar measurements was small, and the average rms difference per wavelength sample varied between 0.7% and 1.7%. Analysis of the results on all flights showed good agreement with the nearly linear dependence of the DOD(pk) with altitude as predicted from calculations based on atmospheric models. The scatter in the relative error of DOD varied with aircraft altitude as expected, and the altitude range with lowest scatter was 8–10 km. Over the entire altitude range the median measurement precision varied from 0.9 to 1.2 ppm. In the optimum altitude range of 8–10 km, most measurements had precisions between 0.2 and 0.9 ppm.

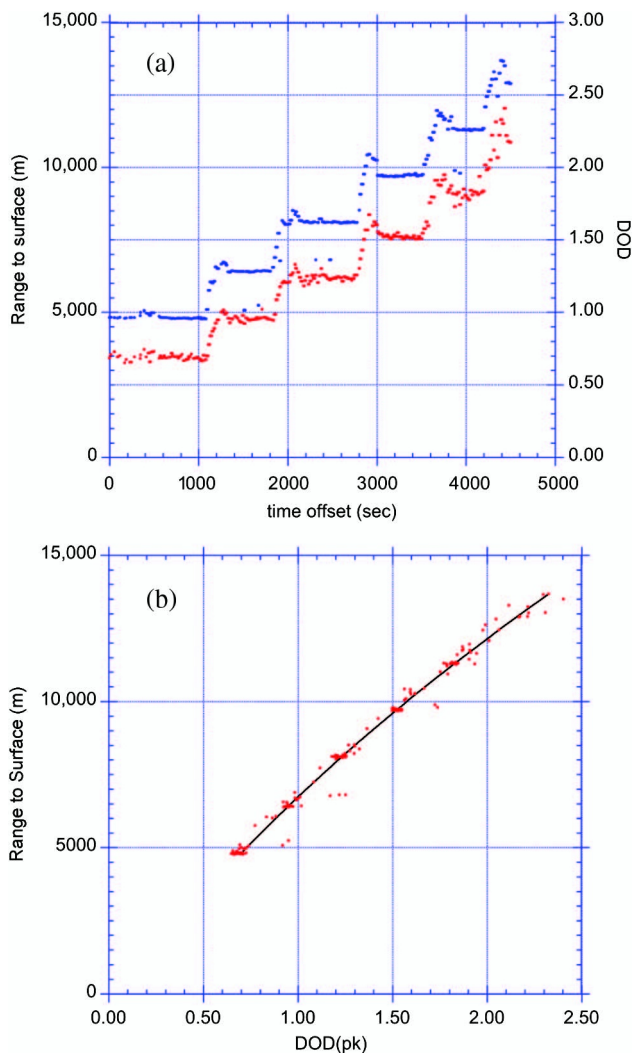


Fig. 14. Measurements from NC flight. (a) Time history of the measured range to the surface (blue dots) and DOD(pk) (red dots). There were 1151 one-second measurements for this flight. (b) Plot of the measured DOD(pk) versus the measured range for the same flight. The line is a best quadratic fit to the measurements.

After these flights we made additional flights on the NASA DC-8 during July 2010 to 13 km altitudes with some instrument modifications, which improved the measurement performance. For these campaigns, the lidar settings were better controlled, which allowed assessments of instrument bias levels. Those measurements have been analyzed [34] and will be reported in the future.

Appendix A: Measurement Model for Random Errors

Here we derive a simplified measurement model to allow evaluating the characteristics of random errors for these airborne measurements. The following discussion is for measurements using only two wavelengths, while our line-scanning approach steps 20 wavelengths across the line shape and uses a least-squares fit of a predicted line shape to the measurements. There are several advantages of the using additional measurement wavelengths distributed across the line. The additional information from the

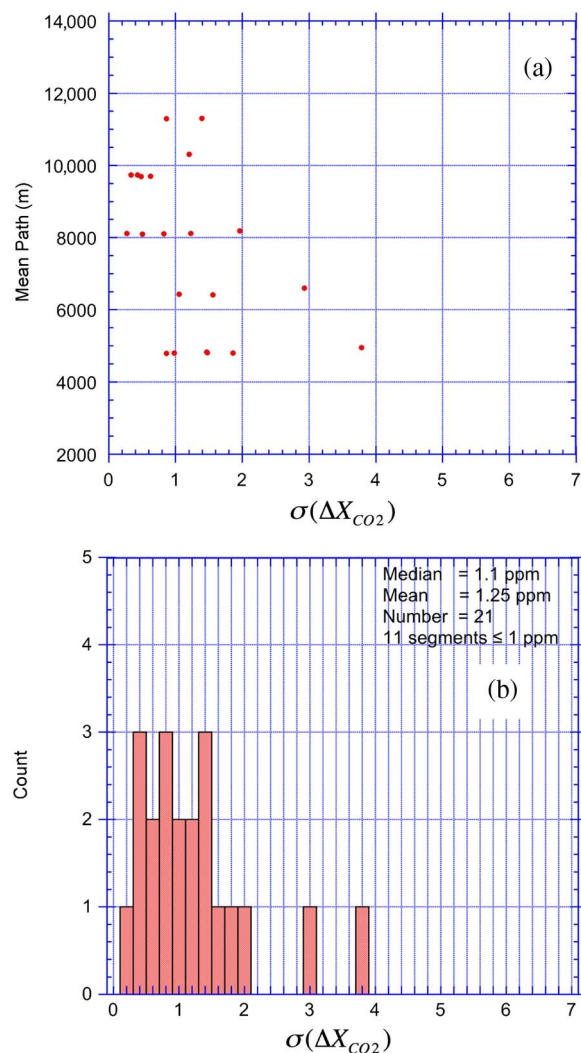


Fig. 15. Analysis for NC flight. (a) Altitude dependence of calculated $\sigma(X_{CO_2})$ for measurements. Measurements were evaluated in groups of 100 s elapsed time and screened only for those groups whose standard deviation (range) is <100 m. Typically each group has ~ 32 measurements. (b) Histogram of the same statistic for measurements at all altitudes. There were 21 groups with a median value of 1.1 ppm, and 11 groups with relative error ≤ 1.1 ppm.

line fit allows solving for spectroscopic shifts of the line with altitude, as well as instrumental offsets, wavelength dependencies, and nonlinearities. Hence the wavelength-distributed approach provides additional information and a significant capability to solve for and thus limit bias errors.

After applying corrections for the solved-for quantities, we have obtained similar results in analyzing random errors to those of the two-wavelength approach if one segments its wavelength-scanned measurements into groups. Combining the signals from the four wavelengths closest to the line center as the on-line, and using the six the measurements nearest the wings (three on the short wavelength side, three on the long) gives similar results [35].

The volume mixing ratio of CO_2 in dry air can be written as

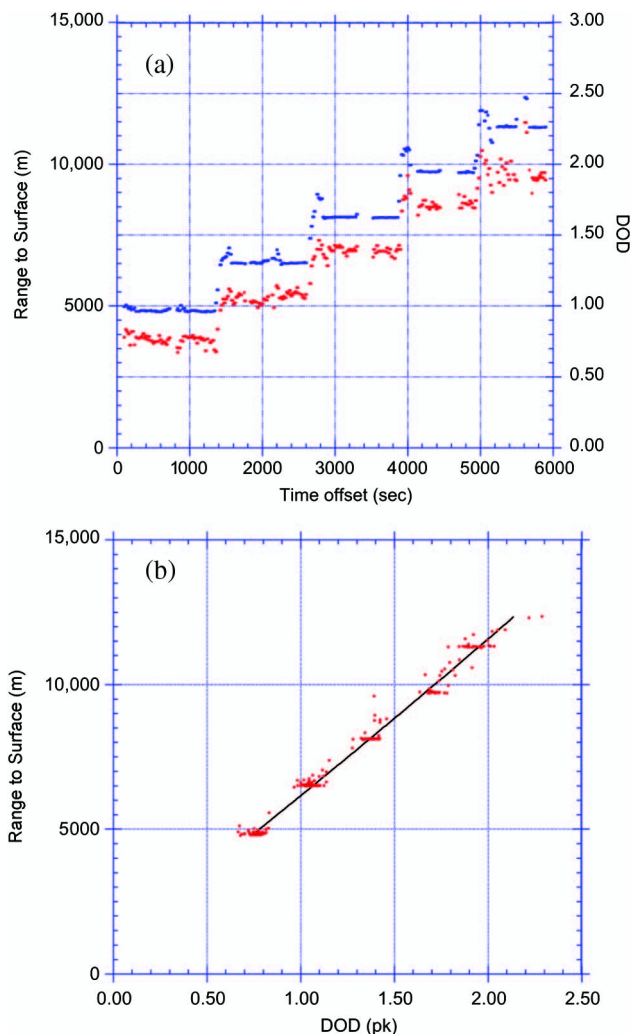


Fig. 16. Measurements from Virginia flight. (a) Time history of the measured range to the surface (blue dots) and DOD(pk) (red dots). (b) Plot of the individual 1 s measured DOD(pk), plotted versus the measured range for the same flight, along with a best quadratic fit to the measurements.

$$X_{\text{CO}_2} = n_1/n_2, \quad (\text{A1})$$

where n is the gas volume density, CO_2 is gas 1 and dry air is gas 2. For our case we have an IPDA lidar that measures the differential absorption in a round-trip pass of the laser beam through the column of CO_2 that extends from ranges 0 to R . For it the two-way transmission, $\tau^2(\lambda, 0, R)$, at wavelength λ_{on} on the peak of the line is related to that at the wavelength λ_{off} in the wing of the line by

$$\tau_1^2(\lambda_{\text{on}}, 0, R) = \tau_1^2(\lambda_{\text{off}}, 0, R) \exp \left\{ -2 \int_0^R [\sigma_1(\lambda_{\text{on}}, r) - \sigma_1(\lambda_{\text{off}}, r)] \times n_1(r) dr \right\}, \quad (\text{A2})$$

where $\sigma_1(\lambda_{\text{on}}, r)$ and $\sigma_1(\lambda_{\text{off}}, r)$ are the respective gas absorption cross sections at location r .

For these experiments we have a nearly vertical nadir-directed path, so $r = z$. We also can set $z = 0$

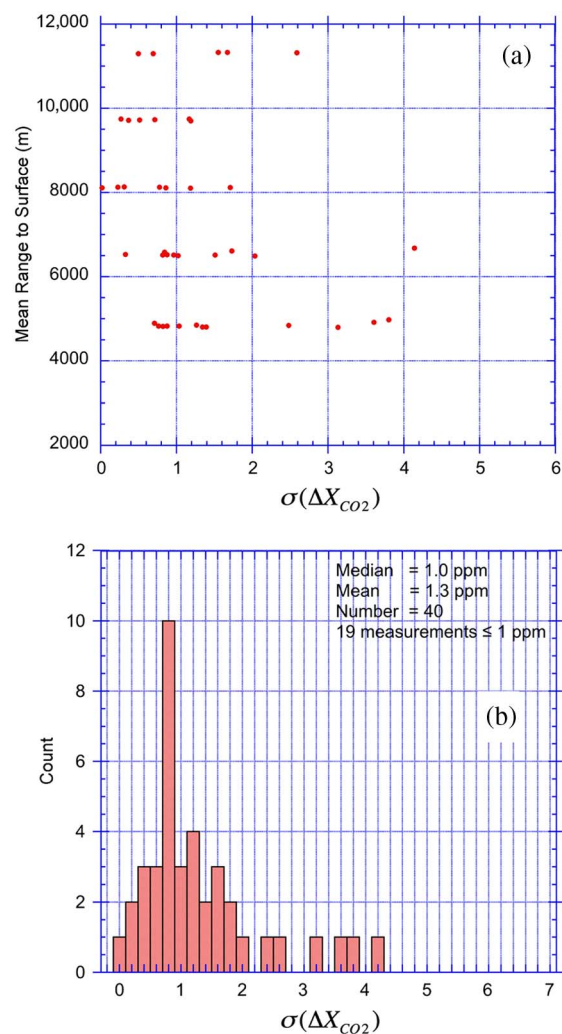


Fig. 17. Analysis for the Virginia flight. (a) Altitude dependence of calculated $\sigma(X_{\text{CO}_2})$ for measurements. Measurements were evaluated in groups of 100 s elapsed time and screened only for those groups whose standard deviation (range) is < 100 m. Typically each group has ~ 32 measurements. The relative errors are minimum at 8–10 km altitudes. (b) Histogram of the same statistic for the groups at all altitudes. There were 40 groups analyzed, the median error was 1.0 ppm, and 19 groups had ≤ 1 ppm error.

to be the elevation of mean sea level (msl) and denote the elevation of the surface relative to msl as z_s . For a vertical measurement from an aircraft at altitude Z to a surface at z_s , the DOD of the CO_2 line can be written as

$$\begin{aligned} \text{DOD}_1(z_s, Z) &= -\ln \left\{ \frac{\tau_1^2(\lambda_{\text{on}}, z_s, Z)}{\tau_1^2(\lambda_{\text{off}}, z_s, Z)} \right\} \\ &= 2 \int_{z_s}^Z [\sigma_1(\lambda_{\text{on}}, r) - \sigma_1(\lambda_{\text{off}}, r)] \times n_1(z) dz \end{aligned} \quad (\text{A3})$$

$$= \text{OD}_{\text{on}}(z_s, Z) - \text{OD}_{\text{off}}(z_s, Z), \quad (\text{A4})$$

Table 3. Summary of 2009 Airborne Measurement Results

Notation	ARM-4	Illinois	North Carolina	Virginia
Center of flight Location	Lamont, OK	Homer, IL	Ahoski, NC	Melfa, VA
Number of 1 s measurements passing screening	1747	1182	1151	2031
<i>DOD(pk) versus range: linear fit results: R</i> value of line fit	0.994	0.989	0.993	0.993
Statistics for groups:				
Number of groups with std dev (range <100 m)	38	16	21	40
Median number of measurements per group	32	32	32	32
Median value of X_{CO_2} statistical error (ppm)	1.2	0.9	1.1	1
Altitude of min values (km)	8–10		8–10	8–10
Minimum value of X_{CO_2} statistical error (ppm)	0.6	0.6	~0.5	~0.5
No. of groups with X_{CO_2} statistical errors ≤ 1 ppm	17	11	11	19
Std dev of range measurements in groups				
Median value (m)	10.1	19.0	16.7	9.8
Minimum value (m)	3.0	4.5	5.1	1.0

where OD_{on} and OD_{off} are the optical depths of the gas absorption at the on and off-line points, respectively.

Equation (A4) was computed versus altitude using a layered atmospheric model for each flight location, and the results are shown in Fig. 8. The plot shows an almost linear dependency of DOD with altitude. To understand this dependency and assess errors, it is helpful to evaluate Eq. (A3) by considering the terms separately. The gas absorption cross section can be written as

$$\sigma_1(\lambda, r) = S_1(r)f_1(\lambda, r), \quad (A5)$$

where $S(r)$ is the absorption line strength. For the 1572.33 nm line used, HITRAN shows that $S(r)$ increases for colder air, and so it increases modestly with higher altitudes. The line shape function f_1 has unit area and depends on $p(r)$ and $T(r)$, the atmospheric pressure, and the temperature at location r . For measurements in the Earth's atmosphere, f_1 can usually be represented as a Voigt line shape. This is a convolution of the Lorentz line shape, caused by pressure broadening, which dominates in the lower atmosphere, and the Doppler line shape, caused by thermal motion of the gas molecules, which dominates in low pressures at higher altitudes.

For these flights, Fig. 6 shows the CO_2 mixing ratio was nearly constant in vertical segments of the atmosphere sampled, so that

$$n_1 \approx X_{CO_2}n_2. \quad (A6)$$

From the ideal gas law, the dry air density varies with altitude as

$$n_2(z) = n_2(0) \frac{p_d(z)}{p_d(0)} \frac{T(0)}{T(z)}, \quad (A7)$$

where p_d is the partial pressure of dry air. The total atmospheric pressure $p = p_d + p_w$, where p_w is the partial pressure of water vapor. This was calculated

from *in situ* measurements during the flights, and the results are plotted in Fig. 6. They show the column average of p_w varied from $0.02 * p_d$ for the lower to $0.005 * p_d$ for the higher flight altitudes; hence for the altitude range of these flights $p \approx p_d$.

As $p(z)$ decreases with altitude, f_1 narrows. Since it has unit area, near the absorption peak, the line shape function value varies inversely with linewidth, so that $f(\lambda_{on}) \propto (T(z))^n / p_d(z)$. Here n is the temperature exponent for the pressure-broadened linewidth, which the HITRAN database gives as $n = 0.67$ for our CO_2 line. The result is that the change in line shape near the peak approximately compensates for $n_2(z)$ decreasing with altitude. So, for this special case, the on-line optical depth

$$OD_{on}(z_s, Z) \approx 2 \int_{z_s}^Z S_1(z) f_i(\lambda_{pk}, 0) \frac{p_d(0)}{p_d(z)} \left[\frac{T(z)}{T(0)} \right]^n \times X_{CO_2} n_2(0) \frac{p_d(z)}{p_d(0)} \frac{T(0)}{T(z)} dz, \quad (A8)$$

which can be simplified to

$$OD_{on}(z_s, Z) \approx 2X_{CO_2}n_2(0) \int_{z_s}^Z S'_1(z) f_i(\lambda_{pk}, 0) dz, \quad (A9)$$

with a temperature-modified line strength

$$S'_1(z) = S_1(z) \left[\frac{T(z)}{T(0)} \right]^{n-1}. \quad (A10)$$

Using these results, Eq. (A8) can be approximated as

$$OD_{on}(z_s, Z) \approx 2(Z - z_s) \bar{\sigma}_1(\lambda_{pk}, 0) X_{CO_2} n_2(0). \quad (A11)$$

Here $\bar{\sigma}_1(\lambda_{pk}, 0) = S'_1(z) f_i(\lambda_{pk}, 0)$ denotes that the temperature-modified cross section is evaluated at the path-averaged temperature but at altitude equal to 0. Although Eq. (A11) is useful for this error analysis, the linear relationship is approximate, due to the increasing value of $S'_1(z)$ with z that causes a slightly

increasing slope of OD with z . This slight curvature is evident in the plots shown in Fig. 8.

The optical depth of the off-line term is

$$\text{OD}_{\text{off}}(z_s, Z) = 2 \int_{z_s}^Z S_1(z) f_i(\lambda_{\text{off}}, z) \times X_{\text{CO}_2 n_2}(0) \frac{p(z) T(0)}{p(0) T(z)} dz. \quad (\text{A12})$$

As shown in Fig. 7, for the λ_{off} chosen, $\text{OD}_{\text{off}} \ll \text{OD}_{\text{on}}$. Computations show its value varies from 5% of OD_{on} near the surface to <1% OD_{on} at the upper flight altitudes. Given its minor role in Eq. (A4), we can replace its cross section by its path-averaged value:

$$\text{OD}_{\text{off}}(z_s, Z) \approx 2(Z - z_s) \sigma_1(\lambda_{\text{off}}, \overline{Z - z_s}) X_{\text{CO}_2 n_2}(0). \quad (\text{A13})$$

Substituting Eqs. (A11) and (A14) into Eq. (A4) yields

$$\text{DOD}_1(z_s, Z) = 2(Z - z_s) [\bar{\sigma}_1(\lambda_{pk}, 0) - \sigma_1(\lambda_{\text{off}}, \overline{Z - z_s})] X_{\text{CO}_2 n_2}(0). \quad (\text{A14})$$

Hence for this case, for a column with approximately a uniform mixing ratio, the DOD also changes approximately linearly with the range to the surface. This result is consistent with the computed values shown in Fig. 8.

From Eq. (A14), the CO_2 volume density at the surface can be determined from measurements of DOD and range by

$$n_1(0) = X_{\text{CO}_2 n_2}(0) = \alpha_1 \frac{\text{DOD}_1(z_s, Z)}{R_1}, \quad (\text{A15})$$

where $\alpha_1 = 1/\{2[\bar{\sigma}_1(\lambda_{\text{on}}, 0) - \bar{\sigma}_1(\lambda_{\text{off}}, \overline{Z - z_s})]\}$ and the range to the surface $R_1 = Z - z_s$.

We are grateful for the support of the NASA Earth Science Technology Office's Advanced Instrument Technology and Instrument Incubator Programs, the NASA ASCENDS Mission Definition activity, and the NASA Goddard IRAD program. We greatly appreciate the work of other members of the Goddard CO_2 Sounder team. We also appreciate the collaborations with James Demers, Alan Mickleright, and Steven Hughell of NASA Glenn, the *in situ* atmospheric measurements from Susan Kooi of NASA LaRC, and the many helpful comments and recommendations from the reviewers.

References

1. P. P. Tans, I. Y. Fung, and T. Takahashi, "Observational constraints on the global atmospheric CO_2 budget," *Science* **247**, 1431–1438 (1990).
2. S. M. Fan, M. Gloor, J. Mahlman, S. Pacala, J. Sarmiento, T. Takahashi, and P. Tans, "A large terrestrial carbon sink in North America implied by atmospheric and oceanic carbon dioxide data and models," *Science* **282**, 442–446 (1998).

3. ESA A-SCOPE Mission Assessment report, http://esamultimedia.esa.int/docs/SP1313-1_ASCOPE.pdf (2008).
4. Z. Kuang, J. Margolis, G. Toon, D. Crisp, and Y. Yung, "Space-borne measurements of atmospheric CO_2 by high-resolution NIR spectrometry of reflected sunlight: an introductory study," *Geophys. Res. Lett.* **29**, 11-1–11-4 (2002).
5. D. M. O'Brien and P. J. Rayner, "Global observations of carbon budget 2, CO_2 concentrations from differential absorption of reflected sunlight in the 1.61 μm band of CO_2 ," *J. Geophys. Res.* **107**, 4354 (2002).
6. A. Kuze, H. Suto, M. Nakajima, and T. Hamazaki, "Thermal and near infrared sensor for carbon observation Fourier-transform spectrometer on the Greenhouse Gases Observing Satellite for greenhouse gases monitoring," *Appl. Opt.* **48**, 6716–6733 (2009).
7. Y. Yoshida, Y. Ota, N. Eguchi, N. Kikuchi, K. Nobuta, H. Tran, I. Morino, and T. Yokota, "Retrieval algorithm for CO_2 and CH_4 column abundances from short-wavelength infrared spectra observations by the Greenhouse gases observing satellite," *Atmos. Meas. Tech.* **4**, 717–734 (2011).
8. E. Dufour and F. M. Breon, "Spaceborne estimate of atmospheric CO_2 column by use of the differential absorption method: error analysis," *Appl. Opt.* **42**, 3595–3609 (2003).
9. J. Mao and S. R. Kawa, "Sensitivity study for space-based measurement of atmospheric total column carbon dioxide by reflected sunlight," *Appl. Opt.* **43**, 914–927 (2004).
10. I. Aben, O. Hasekamp, and W. Hartmann, "Uncertainties in the space-based measurements of CO_2 columns due to scattering in the Earth's atmosphere," *J. Quant. Spectrosc. Radiat. Transfer* **104**, 450–459 (2007).
11. United States National Research Council, "Earth science and applications from space: national imperatives for the next decade and beyond," <http://www.nap.edu/> (2007).
12. NASA ASCENDS Mission Science Definition and Planning Workshop Report, http://cce.nasa.gov/ascends/12-30-08%20ASCENDS_Workshop_Report%20clean.pdf (2008).
13. Y. Durand, J. Caron, P. Bensi, P. Ingmann, J. Bézy, and Meynart, "A-SCOPE: concepts for an ESA mission to measure CO_2 from space with a lidar," in *Proceedings of the 8th International Symposium on Tropospheric Profiling*, Delft, The Netherlands, 18–23 October 2009.
14. G. Ehret, C. Kiemle, M. Wirth, A. Amediek, A. Fix, and S. Houweling, "Space-borne remote sensing of CO_2 , CH_4 , and N_2O by integrated path differential absorption lidar: a sensitivity analysis," *Appl. Phys. B* **90**, 593–608 (2008).
15. J. Caron and Y. Durand, "Operating wavelengths optimization for a spaceborne lidar measuring atmospheric CO_2 ," *Appl. Opt.* **48**, 5413–5422 (2009).
16. R. Measures, *Laser Remote Sensing: Fundamentals and Applications* (Krieger, 1992), pp. 205–213.
17. C. Weitkamp, *Lidar: Range Resolved Optical Remote Sensing of the Atmosphere* (Springer, 2005), pp. 187–238.
18. J. B. Abshire, H. Riris, G. R. Allan, C. J. Weaver, J. Mao, X. Sun, W. E. Hasselbrack, S. R. Kawa, and S. Biraud, "Pulsed airborne lidar measurements of atmospheric CO_2 column absorption," *Tellus Ser. B* **62**, 770–783 (2010).
19. G. Spiers, R. Menzies, J. Jacob, L. Christensen, M. Phillips, Y. Choi, and E. Browell, "Atmospheric CO_2 measurements with a 2 μm airborne laser absorption spectrometer employing coherent detection," *Appl. Opt.* **50**, 2098–2111 (2011).
20. H. Riris, J. Abshire, G. Allan, J. Burris, J. Chen, S. Kawa, J. Mao, M. Krainak, M. Stephen, S. Wilson, and E. Wilson, "A laser sounder for measuring atmospheric trace gases from space," *Proc. SPIE* **6750**, 67500U (2007).
21. G. R. Allan, H. Riris, J. B. Abshire, X. Sun, E. Wilson, J. F. Burris, and M. A. Krainak, "Laser sounder for active remote sensing measurements of CO_2 concentrations," in *Proceedings of 2008 IEEE Aerospace Conference* (IEEE, 2008), pp. 1534–1540.
22. J. B. Abshire, H. Riris, G. R. Allan, C. J. Weaver, J. Mao, X. Sun, W. E. Hasselbrack, A. Yu, A. Amediek, Y. Choi, and E. V. Browell, "A lidar approach to measure CO_2 concentrations from space for the ASCENDS Mission," *Proc. SPIE* **7832**, 78320D (2010).

23. A. Amediek, X. Sun, and J. B. Abshire, "Analysis of range measurements from a pulsed airborne CO₂ integrated path differential absorption lidar," *IEEE Trans. Geosci. Remote Sens.* **51**, 2498–2504 (2013).
24. M. Stephen, M. Krainak, H. Riris, and G. R. Allan, "Narrow-band, tunable, frequency-doubled, erbium-doped fiber-amplified transmitter," *Opt. Lett.* **32**, 2073–2076 (2007).
25. M. A. Stephen, J. Mao, J. B. Abshire, S. R. Kawa, X. Su, and M. A. Krainak, "Oxygen spectroscopy laser sounding instrument for remote sensing of atmospheric pressure," in *IEEE Aerospace Conference* (IEEE, 2008), pp. 1–6.
26. J. Mao, S. R. Kawa, J. B. Abshire, and H. Riris, "Sensitivity studies for a space-based CO₂ laser sounder," in *Transactions of the American Geophysical Union*, Vol. **88** (2007), abstract A13D-1500.
27. X. Sun and J. Abshire, "Comparison of IPDA lidar receiver sensitivity for coherent detection and for direct detection using sine-wave and pulsed modulation," *Opt. Express* **20**, 21291–21304 (2012).
28. NASA-Glenn Lear-25, airbornescience.nasa.gov/aircraft/learjet **25** (2010).
29. Y. Choi, S. A. Vay, K. P. Vadevu, A. J. Soja, J.-H. Woo, S. R. Nolf, G. W. Sachse, G. S. Diskin, D. R. Blake, N. J. Blake, H. B. Singh, M. A. Avery, A. Fried, L. Pfister, and H. E. Fuelberg, "Characteristics of the atmospheric CO₂ signal as observed over the conterminous United States during INTEX-NA," *J. Geophys. Res.* **113**, D07301 (2008).
30. S. Vay, J. Woo, B. Anderson, K. L. Thornhill, D. R. Blake, D. J. Westberg, C. M. Kiley, M. A. Avery, G. W. Sachse, D. G. Streets, Y. Tsutsumi, and S. R. Nolf, "Influence of regional-scale anthropogenic emissions on CO₂ distributions over the western North Pacific," *J. Geophys. Res. Atmos.* **108**, 27 (2003).
31. C. Rodgers, *Inverse Methods for Atmospheric Soundings, Theory and Practice*, Vol. **2** of Series on Atmospheric, Oceanic and Planetary Physics (World Scientific, 2000), p. 238.
32. L. S. Rothman, I. E. Gordon, A. Barbe, D. ChrisBenner, P. F. Bernath, M. Birk, V. Boudon, L. R. Brown, A. Campargue, J. P. Champion, K. Chance, L. H. Coudert, V. Danaj, V. M. Devi, S. Fally, J. M. Flaud, R. R. Gamache, A. Goldman, D. Jacquemart, I. Kleiner, N. Lacome, W. J. Lafferty, J. Y. Mandin, S. T. Massie, S. N. Mikhailenko, C. E. Miller, N. Moazzen-Ahmadi, O. V. Naumenko, A. V. Nikitin, J. Orphal, V. I. Perevalov, A. Perrin, A. Predoi-Cross, C. P. Rinsland, M. Rotger, M. Šimečková, M. A. H. Smith, K. Sung, S. A. Tashkun, J. Tennyson, R. A. Toth, A. C. Vandaele, and J. VanderAuwera, "The HITRAN 2008 molecular spectroscopic database," *J. Quant. Spectrosc. Radiat. Transfer* **110**, 533–572 (2009).
33. X. Sun and J. B. Abshire, "Receiver performance analysis of a photon counting laser sounder for measuring atmosphere CO₂ concentration," in *ILRC-25 Conference Proceedings* (Curran Associates, 2011), pp. 1320–1323.
34. J. Abshire, H. Riris, G. Allan, X. Sun, J. Mao, C. Weaver, A. Yu, J. Chen, M. Rodriguez, and S. Kawa, "Pulsed lidar for measurements of CO₂ concentrations for the ASCENDS mission," in *NASA ESTF 2011 Conference*, Pasadena, California (June 2011), paper B8P1. Available from http://esto.nasa.gov/conferences/estf2011/presentations/Abshire_ESTF2011.pdf.
35. X. Sun, NASA Goddard, private communication (2012).